Nanoscale Advances

ROYAL SOCIETY OF CHEMISTRY

PAPER

View Article Online
View Journal | View Issue

Cite this: *Nanoscale Adv.*, 2025, **7**, 5212

UV-SERS monitoring of plasmonic photodegradation of biomolecules on aluminum platforms decorated with rhodium nanoparticles†

Yanqiu Zou,[a] Luca Mattarozzi,[b] Huaizhou Jin,[c] Qifei Ma,[d] Sandro Cattarin,[b] Shukun Weng,[e] Ali Douaki,[e] German Lanzavecchia,[e] Karol Kołątaj,[f] Nicco Corduri,[f] Ben Johns,[gh] Nicolò Maccaferri,[gh] Guillermo Acuna,[f] Zhenrong Zheng,*[a] Shangzhong Jin*[d] and Denis Garoli*[ei]

Received 16th May 2025
Accepted 6th July 2025

DOI: 10.1039/d5na00486a

rsc.li/nanoscale-advances

In the search for novel nanostructured materials for UV plasmonics, only a limited number of choices are available. Materials such as aluminum, rhodium, and gallium can be used. One of the most interesting applications of UV plasmonics is surface-enhanced Raman spectroscopy. It can be extended to this spectral range to explore the spectral properties of biomolecules that have only a small cross-section in the visible spectral range. We have recently reported on a functional substrate based on nanoporous aluminum decorated with rhodium nanoparticles. This system exhibited an interesting behavior with UV excitation at 266 nm and an unexpected decrease in Raman intensity with an increase in rhodium nanoparticle concentration. We proposed that this effect can be due to the difficult access of the molecules deposited *via* thermal evaporation to hot spots. Herein, we extend the above-mentioned study by exploring the performance of the system at another UV excitation wavelength of 325 nm and by reporting experimental results obtained using a deposition process that can bring the molecules to the hot spots in a more efficient way. Extensive spectroscopic data, combined with 3D maps, provided a more clear view of the performance of this plasmonic platform. In particular, the photodegradation and potential oxidation of biomolecules driven by the hot electrons/hot holes produced by the rhodium nanoparticles are reported.

Introduction

Surface plasmon resonance finds extensive applications in multiple fields such as metal-enhanced fluorescence (MEF), photocatalysis, optical trapping, heating, energy harvesting and surface-enhanced Raman spectroscopy (SERS).[1,2] The latter, in particular, has been the subject of intensive research that enabled to demonstrate, in the most recent years, the possibility to obtain Raman spectra from single molecules and to investigate, with a temporal resolution of few milliseconds, the molecular dynamics in chemical reactions.[1,2] Nowadays, SERS platforms are still based on noble metals (Au and Ag), and their application is typically limited to the visible/near-infrared (Vis/NIR) spectral range. As is well known, metals such as aluminum, magnesium, rhodium and gallium can be used to prepare plasmonic platforms working in the spectral range of UV and deep-UV wavelengths.[3,4] The excitation of biomolecules using UV radiation is particularly interesting for Raman spectroscopy. In fact, most biomolecules have small Raman cross-sections in the visible and NIR regions,[5,6] and the use of higher energy to excite them can increase the detection limit because of the presence of electronic resonances.[7–11] Aluminum (Al) is the most extensively explored material for UV plasmonics considering its excellent electrical properties,[12] which facilitate significant resonance in the UV range. In order to apply aluminum's plasmonic characteristics in SERS, very small metallic structures/nanostructures must be prepared by means of advanced lithographic techniques or chemical synthesis of nanoparticles.[13–15] As an alternative approach to produce metals with nanometer features, the preparation of Al films as nanoporous materials (NPMs)[16–19] has been recently reported with

[a]State Key Laboratory of Modern Optical Instrumentation, College of Optical Science and Engineering, Zhejiang University, Hangzhou 310027, China. E-mail: zzr@zju.edu.cn
[b]ICMATE - CNR, Corso Stati Uniti 4, 35127 Padova, Italy
[c]Key Laboratory of Quantum Precision Measurement, College of Physics, Zhejiang University of Technology, Hangzhou, China
[d]College of Optical and Electronic Technology, China Jiliang University, Hangzhou 310018, China. E-mail: denis.garoli@unimore.it
[e]Istituto Italiano di Tecnologia, via Morego 30, I-16163, Genova, Italy
[f]Department of Physics, University of Swiss National Center for Competence in Research (NCCR) Bio-inspired Materials, University of Fribourg, CH-1700 Fribourg, Switzerland
[g]Department of Physics, Umeå University, Linnaeus väg 24, 901 87 Umeå, Sweden
[h]Umeå Centre for Microbial Research, Umeå, 901 87, Sweden
[i]Dipartimento di Scienze e Metodi dell'Ingegneria, Università degli Studi di Modena e Reggio Emilia, Via Amendola 2, Reggio Emilia, 42122, Italy

† Electronic supplementary information (ESI) available. See DOI: https://doi.org/10.1039/d5na00486a

the experimental demonstration of efficient UV-MEF and UV-SERS.[6,20,21] Porous Al structures can be prepared following different strategies.[6,22]

Another intriguing approach towards advanced plasmonic platforms involves the combination of two or more plasmonic materials in the same system.[23,24] In UV-SERS, in particular, the use of rhodium (Rh)[7,25–28] combined with Al could represent an interesting platform to better comprehend how to produce strongly localized electromagnetic fields in the UV spectral range. Therefore, porous Al can be decorated with Rh *via* a galvanic displacement (GD) reaction, which allows the reproducible preparation of metallic nanoparticles of a more noble metal spontaneously, at the open circuit, with the use of simple chemical apparatus.[29]

For this reason, we have recently reported on the facile and low-cost fabrication of porous Al substrates decorated with Rh nanoparticles (NPs).[30] It is noteworthy that the current main limitation of Rh use in the preparation of plasmonic devices is the very high material cost. The methodology proposed herein allows a significant coverage by Rh NPs using minimal Rh amounts. By studying this system for UV-SERS (probing adenine with an excitation laser at 266 nm), we observed two interesting phenomena: (i) increasing the density of Rh NPs over the porous Al substrate leads to a decrease in the SERS enhancement and (ii) the Rh NPs slow down the UV-induced photodegradation effect observed during long acquisition time.

In this work, we extended the investigations on this plasmonic platform by performing additional SERS analyses using a laser source at 325 nm to excite and probe two biomolecules, *i.e.* adenine and bovine serum albumin (BSA), drop-casted from water-based solutions. In particular, adenine is a major contributor to the SERS features of DNA oligomers and strands;[31] therefore, it is still important to investigate SERS processes on this molecule, in particular in the UV spectral range. We discuss on the photodegradation process induced by the UV exposure considering also the potential effect of progressive oxidation of adenine to azupurine, as previously demonstrated in photoelectrochemical experiments.[32] The progressive oxidation of adenine resulted to be more pronounced for higher Rh NPs contents.

In addition to these analyses, we report on the excitation of BSA discussing both the ability of the platform to detect the main Raman peaks and the photostability of the molecule after multiple UV exposures. It is well known that serum albumin is the most abundant protein in vertebrate blood and plays an important role as a carrier and in interacting with external molecules and materials. In the study of this protein, deep UV (around 200 nm)[33] was typically used for resonant Raman excitation, and the selective enhancement of the signals of amide vibrations occurs, enabling the characterization of the protein secondary structure. Herein, we discuss the excitation out of molecular resonance using the UV wavelength at 325 nm.

Results and discussion

To conduct the UV-SERS experiments, we used a new set of samples prepared following a procedure similar to the one reported in our recent publication.[30] Table 1 reports the conditions of GD procedures on Al substrates.

Table 1 Experimental conditions for sample preparation

Sample ID	GD bath	t_{GD} min	Surface Rh coverage %
a	—	0	0
b	0.5 mM Na_3RhCl_6 + 0.09 M NaCl	2	6.46
c	0.5 mM Na_3RhCl_6 + 0.09 M NaCl	4	11.49

Fig. 1(A–C) illustrate the SEM micrographs obtained for samples a–c, while Fig. 1(D) reports the coverage of Rh NPs (%) with respect to the corresponding galvanic displacement times. Specifically, sample b (t_{GD} = 2 min) exhibited a Rh NP coverage of 6.46 ± 0.64%, translating to 3.73 ± 0.37 particles per μm^2 with a mean radius of 74 ± 18 nm, and Sample *c* (t_{GD} = 4 min) showed a coverage of 11.49 ± 1.23%, corresponding to 8.59 ± 0.89 particles per μm^2 with a mean radius of 65 ± 20 nm. These quantitative measurements provide a clearer comparison of Rh NP densities across different galvanic displacement durations. All samples display a significantly roughened Al surface decorated with different concentrations of randomly distributed Rh NPs. With respect to the previous report,[30] no mechanical polishing was executed on the Al substrates to avoid surface damages due to mechanical scratching and inclusions of silicon carbide particles used for the polishing. The pristine surface of the Al exposed to Rh^{3+} ions reacted, facilitating the preparation of Rh NPs with a reduced size distribution (see ESI #1†). The cross-section imaging allows observing that the NPs present a morphology approaching a hemi-spherical shape. To verify the electromagnetic field configurations that can be produced

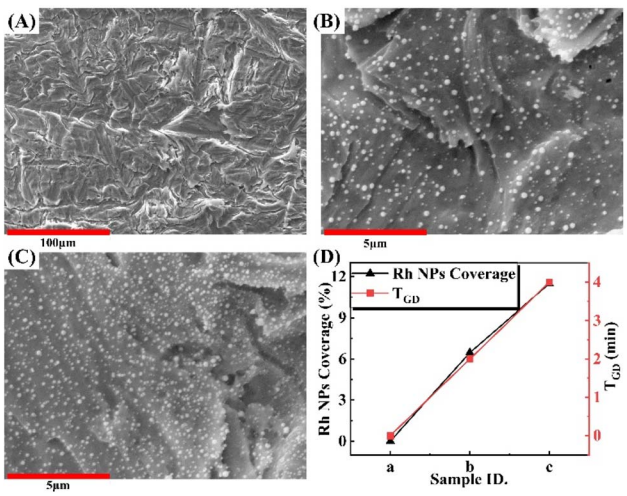

Fig. 1 Details of the prepared samples. SEM images of (A) untreated rough Al (sample a, no GD) and (B–C) Al samples subjected to galvanic displacement in 0.5 mM Na_3RhCl_6, pH 2.0, for different times: (B) t_{GD} = 2 min (sample b); (C) t_{GD} = 4 min (sample c), magnified detail. (D) Line chart depicting Rh NP coverage (%) for samples a–c at corresponding galvanic displacement times, showing 6.46% for sample b and 11.49% for sample c.

by such structures, we performed numerical simulations using Comsol Multiphysics. The details of the simulations and the results are illustrated in ESI #2,† where we considered two "partial-dome" configurations for the NPs on the Al substrate. We find a strongly enhanced electric field around the Rh NPs, particularly near the gap between single Rh NPs and the Al substrate.

With respect to the previous experiments,[30] here two main points were modified, *i.e.* the procedure to deposit the target analyte (adenine and BSA[34–36]) and the excitation wavelength used in the Raman spectroscopy (325 nm). In particular, while in the previous case the samples were coated with the probe molecules by means of physical vapor deposition, here we tested molecules in solution. By using this approach, we expect to achieve a more efficient interaction between the molecules and the gap between the single Rh NPs and the Al substrate, where the electromagnetic field is more localized.[30]

We focused our experiments on the investigation of the photodegradation processes of adenine and BSA due to successive UV laser exposures. In order to do that, we first measured all the samples functionalized with adenine (using a concentration of 0.5 mM). We performed six successive scans over an area of $2 \times 2\ \mu m^2$. The adenine spectra obtained from all the samples are shown in Fig. 2, showing clearly distinguishable bands that correspond to the molecular vibrations of adenine, as previously reported in resonant Raman experiments with adenine and related compounds, as well as in pre-resonant SERS spectra on Rh composite materials.[37–41] Fig. 2(A) illustrates a direct comparison between the samples after a first single laser scan, while Fig. 2(B) depicts the maximum intensity around 731 cm^{-1} and 1331 cm^{-1} for the tested samples. The position of the obtained spectral peaks exhibited shifts. We provide an explanation in ESI #3, Fig. S5(a), S6(a) and (d).† Fig. 2(C–D) report the relative 3D time-dependent UV-SERS spectra and mean spectra of adenine across six consecutive scans on sample a, respectively, clearly showing the photodegradation due to successive UV exposures. We also present the average UV-SERS spectra of adenine from six consecutive scans on sample b and c in ESI #3, Fig. S5(c) and S5(d),† respectively.

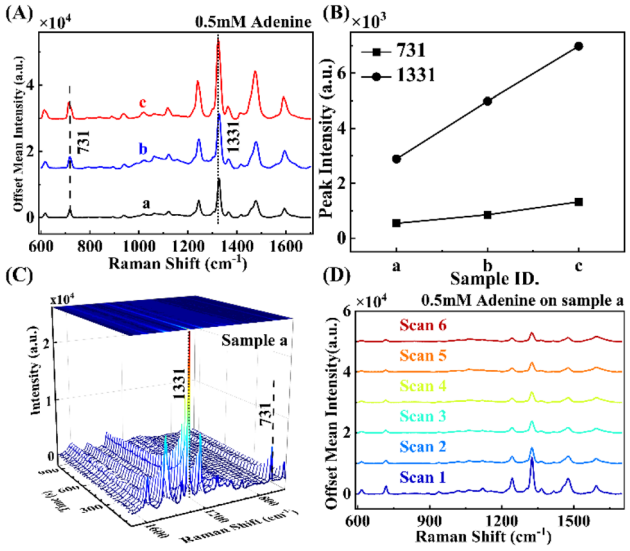

Fig. 2 Adenine UV-SERS spectra from Al–Rh NP samples. (A) Comparison between the first scans obtained from the three tested samples. (B) Maximum values around 731 cm^{-1} and 1331 cm^{-1} extracted from the spectra in (A). (C and D) 3D time-dependent SERS spectra and mean SERS spectra across six consecutive scans of 0.5 mM adenine on sample a.

As a first important observation, the intensities of the UV-SERS spectrum resulted in an increase with the increase in Rh contents on the samples, as detailed in Table 1 and illustrated in Fig. 1(D). Fig. 2(B) shows that the increase in Rh NP coverage percentages is generally positively correlated with SERS signal intensities at both wavenumbers, with the Pearson correlation coefficient being slightly lower at 1331 cm^{-1} ($r = 0.75$) compared to 731 cm^{-1} ($r = 0.81$). Specifically, sample c (Rh NP coverage = 11.49%) exhibited the highest SERS intensities at both wavenumbers, while sample a, without GD treatment, served as a control and demonstrated the lowest SERS signal intensities. This is partially in disagreement with our previous results,[30] where the Rh NPs seemed to reduce the intensity of the Raman peaks. As already reported, this is due to the inefficient interaction between the plasmonic hot spots generated by the NPs and the physical evaporated probe molecules. Here, on the contrary, the molecules can interact uniformly with the whole sample thanks to the functionalization method used.

In all the measurements, the two most characteristic SERS peaks of adenine at around 731 and 1331 cm^{-1} were identified.[32,42] However, there are several other strong bands that appear between 1000 and 1500 cm^{-1}, such as 1048, 1423, and 1482 cm^{-1}. The first observation of this kind of SERS spectrum was reported for adenosine on a roughened silver electrode at a positive potential in 1985.[43] We also conducted the SERS spectra of several derivatives of adenine in ESI #4.† As shown in Fig. S7,† the results indicated that we can observe a vibrational band for adenine and its derivatives NAD^+, ATP and adenosine within the wavenumbers of 1000 and 1100 cm^{-1}, similar to the literature report,[32] but the peak also shows different shifting to around 1070 cm^{-1}.

As a first step in the photodegradation analyses, we monitored the intensity of the peak at 1331 cm^{-1} during six mapping scans over the different samples. The mode at 1331 cm^{-1} corresponds to a skeletal vibration of the pyrimidine ring,[44] and its intensity could therefore be indicative of the decomposition of the molecule. The decrease in intensity of this band could indicate the dissociation of skeletal purine ring bonds and/or re-orientation of the molecule on the nanostructure.

For each map, we selected the intensity at 16 points and normalized the intensities to the range [0, 1]. Fig. 3(A–C) show the scatter diagram of the data with the fit curve obtained across samples a–c using the following formula:

$$y = y_0 + A_1 e^{-t/t_1} \quad (1)$$

where y_0 is the initial intensity, y is the current intensity, t is the time, and t_1 is the time constant associated with the degradation rate $k = 1/t_1$. It can be observed that the root mean square

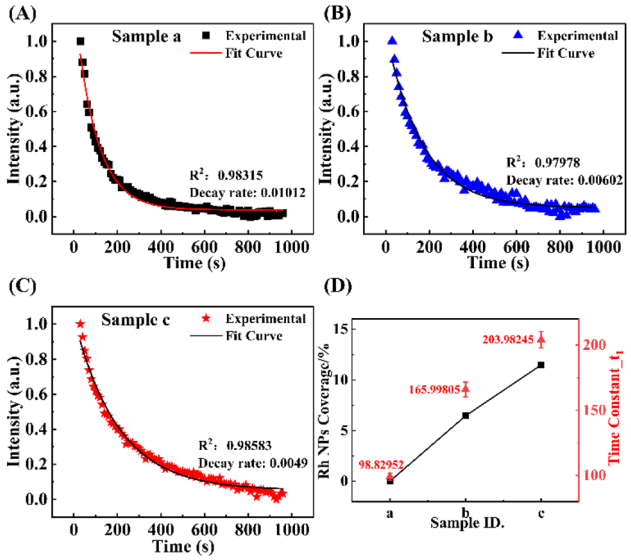

Fig. 3 (A–C) Experimental data and corresponding photodegradation fitting curves of peak intensity at around 1331 cm^{-1} for adenine as a function of collection time for different samples a–c, respectively. (D) Time constants of sample a–c with varying Rh NPs coverage percentages.

errors (RMSEs) of the fits for different samples are all greater than 0.97, indicating that the degradation process respects eqn (1). The degradation rate for the three samples is also marked in Fig. 3(A–C). Sample a without GD treatment exhibited the highest decay rate (0.01011 s^{-1}), while sample b and c demonstrated lower decay rates of 0.00602 s^{-1} and 0.0049 s^{-1}, respectively, indicating that a higher Rh NPs content effectively reduces the degradation rate, which is in agreement with our previous results.[30] Fig. 3(D) illustrates the time constants measured for three samples with different Rh NP coverage percentages. Specifically, sample a with no GD treatment exhibited a time constant of 98.83 ± 2.82 s, sample b with 6.46% coverage had a time constant of 165.99 ± 5.70 s, and sample c with 11.49% coverage demonstrated a time constant of 203.98 ± 6.30 s. The increase in time constants is correlated with the increasing coverage of Rh NPs, indicating enhanced stability or altered kinetics under varying nanoparticle coverage percentages.

As reported by Su *et al.*,[32] the peaks of adenine at 732 cm^{-1} and 1333 cm^{-1} are regular peaks, while the peaks that can be observed at 1048 cm^{-1}, 1423 cm^{-1}, and 1482 cm^{-1} are defined as unusual peaks. These unusual Raman peaks are attributed to adenine derivatives or oxidation products. It is known that UV light induces photochemical reactions on adenine.[45,46] Nonetheless, plasmonic nanostructures can, in principle, contribute to the oxidation process of adenine to azupurine *via* hot carrier generation.[32] In particular, the peaks associated with azupurine formation are exactly in the spectral range between 1048 and 1480 cm^{-1}, as observed in our experiments. Therefore, after normalizing the different peaks, we first examined the overall changes in the other peaks with increasing scan time to determine whether they behaved similarly to the peak at 1331 cm^{-1}. We reported these analyses in ESI #5.† The obtained degradation time constant for the three samples under four Raman-active wavelengths is reported in Table 2, each accompanied by its standard error. By combining the Rh NP coverage percentages presented in Table 1 and the time constants under 1331 cm^{-1} related to the Rh NPs contents shown in Fig. 3(D), we can conclude that Rh incorporation generally improves photostability, as evidenced by the increased t_1 values in samples with higher Rh NPs contents.

Specifically, the standard deviations at 1331 cm^{-1} and 1482 cm^{-1} are both less than 10, which indicates that the fitting results are in good agreement with eqn (1). Sample c (11.49% Rh NPs coverage) showed the highest t_1 values at 1331 and 1482 cm^{-1}, while Sample a, with no Rh content, exhibited the lowest t_1 values, suggesting that Rh contributes significantly to photostability. However, for the photodegradation constants of adenine at the fitted peaks of 1048, 1423 and 1067 cm^{-1}, samples containing Rh NPs generally exhibit large standard error values and even anomalies. This indicates that using photodegradation eqn (1) alone is no longer sufficient to meet the fitting convergence conditions. Moreover, these peaks are roughly classified as "unusual peaks" as defined in ref. 32. For unusual peaks, further analyses are necessary.

In order to better understand the potential oxidation reaction from adenine to azupurine, additional data analyses on the collected spectra were performed by calculating the area ratio between different spectral ranges. The results calculated using Python are presented in ESI #6 Fig. S9,† which demonstrate that peak areas in the [700, 745] cm^{-1} range initially decrease and then stabilize, the [1285, 1352] cm^{-1} range exhibit a gradual reduction slowed by Rh nanoparticles, and the [960, 1200] cm^{-1} range generally decrease with the increase in scans, accompanied by ratio analyses indicating consistent normal peak ratios and varying relative changes in other peak ratios.

To investigate whether Rh NPs have an oxidation effect on adenine and alter the "unusual peak" of adenine around ranges of 1000 to 1100 cm^{-1} (according to the literature, silver colloid-induced visible adenine SERS exhibits oxidation effects on

Table 2 Calculated photodegradation time constants (t_1) for the three samples across various wavenumbers

	Time constant (t_1) under different wavelength			
ID	1048 cm^{-1}	1067 cm^{-1}	1423 cm^{-1}	1482 cm^{-1}
a	75.3 ± 14.7 (s)	69.3 ± 8.3 (s)	105.1 ± 8.8 (s)	101.6 ± 3.6 (s)
b	90.5 ± 25.9 (s)	96.4 ± 21.5 (s)	118.3 ± 18.7 (s)	137.3 ± 8.4 (s)
c	543.2 ± 148.9 (s)	−485.2 ± 279 (s)	226.7 ± 23.2 (s)	221.3 ± 7.7 (s)

characteristic peaks around 1048 cm^{-1}),[32] we performed multiple peak deconvolution on the [960, 1200] cm^{-1} range and single peak fitting on the [700, 745] cm^{-1} range by applying Gaussian functions, using the following formula:[47]

$$y = y_0 + \frac{A e^{\frac{-4\ln(2)(x-x_c)^2}{w^2}}}{w\sqrt{\frac{\pi}{4\ln(2)}}} \quad (2)$$

where x_c is the center peak wavenumber, setting the initial value $y_0 = 0$. Fig. S10 in ESI #7† displays the fit curve of sample as an example to illustrate our reporting method. Using eqn (2), we performed the peak fitting and calculated the corresponding area and relative full width at half maximum (FWHM). Since the area corresponding to the wavenumber range of [700–745] cm^{-1} does not change significantly with an increasing number of scans, we selected the fitting peak at approximately 731 cm^{-1}. We then calculated the ratio of the peak area for each fitted peak to the peak area around 731 cm^{-1} obtained from the same spectrum. The calculation results are shown in ESI #7, Fig. S11,† which report the variation in the peak area corresponding to the fitting peak with the number of scans. The results show that the ratio of the fitted peak areas increases as the number of scans increases. When combined with the Rh NPs coverage percentage presented in Table 1, we can observe how higher concentrations of Rh NPs seem to promote greater oxidation effects, as evidenced by the steeper slopes observed at around 1075 cm^{-1} fitted peak, which is indicative of enhanced oxidative interactions within the sample matrix, as reflected in the altered SERS peak area ratios within the 1000–1100 cm^{-1} range. It is interesting to note that this oxidation process seems to be not accompanied by the oxidation of carbon species on the samples' surface. In fact, even after multiple laser scans, we did not observe any increasing peak intensity around 1600 cm^{-1}, where the main carbon oxide vibration is expected.[48,49]

UV-SERS experiments using adenine as a probe molecule have been reported in several papers.[5,6,15,22,30,46] On the contrary, measurements on proteins were not so extensively discussed.[33,50] Here we test our substrate also as a platform for UV-SERS using BSA, a protein whose SERS spectroscopy has been previously reported.[51–53]

We first tested the bulk BSA on silica chip, and the corresponding result is reported in ESI #9, Fig. S12.† Then we measured the Al–Rh NPs substrates using 15.1 μM BSA concentration in water solution and we performed multiple scans over the same area to evaluate the effect of successive UV exposures.

Fig. 4 reports the spectrum obtained after a single scan from the different samples and illustrates the relative changes in the intensity ratios of the peak between 1050 and 1070 cm^{-1} and 1500 and 1700 cm^{-1} in the UV-SERS spectra of BSA across four consecutive scans on different substrates (a–c). As can be seen, with respect to adenine, in this case only few peaks can be detected. In particular, the relatively broad peaks at around 1606, 1360 and at 1064 cm^{-1} can be associated with the vibration of BSA in agreement with previous reports.[33,34,50,51]

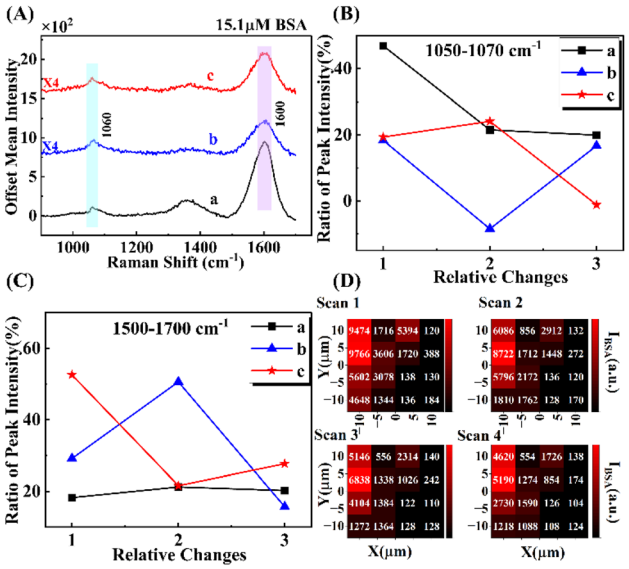

Fig. 4 UV-SERS on different samples a–c (black, blue and red spectra, respectively) with 15.1 μM BSA and peak intensity analysis. (A) Mean intensity. (B–C) Ratios of peak intensity changes across four scans for Rh-modified Al ranging from 1050 to 1070 cm^{-1} and 1500 to 1700 cm^{-1}. (D) Mapping images of sample a across four scans in the range between 1500 and 1700 cm^{-1}.

Notably, here the excitation laser at 325 nm is not in resonance with the molecule, therefore we were able to detect only a small number of vibrations with respect to other reports where the resonant Raman was obtained using higher frequencies for the laser excitation.[50] In this case, it is not easy to assign the peak position to clear molecular vibrations. In particular, the peak at 1600 cm^{-1} could be assigned to the presence of carbon oxide species on the substrate surface, even if we did not observe an increasing intensity for successive scans and we did not observe this carbon vibration in the multiple Raman experiments performed with adenine.

Sample a (black line in Fig. 4(A)), which does not contain Rh NPs, exhibits the strongest BSA Raman enhanced signal and a broad peak around 1360 cm^{-1}. The relative peak intensity in the range between 1050 and 1070 cm^{-1} and 1500 and 1700 cm^{-1} of BSA UV-SERS spectra evaluated across three scan intervals (labeled 'relative changes' as x-axis) for three samples was reported in Fig. 4(B) and (C), respectively. Taking the Rh NPs coverage percentage in Table 1 into account, we can conclude that Rh NPs exert some concentration-dependent effects on the vibrational dynamics of the system. Specifically, the 1600 cm^{-1} peak in Fig. 4(C) exhibits a significant initial enhancement in samples with the Rh NPs content, especially in sample c, where the intensity ratio reaches 52.55% after the first scan. Subsequently, the intensity ratio decreases and slightly rebounds in the following scans, reflecting rapid structural changes and subsequent reaction dynamics catalysed by Rh NPs. In contrast, the 1060 cm^{-1} peak in Fig. 4(B) continuously decreases in the Rh NP-free sample a, whereas in samples with Rh NPs, it shows a complex trend. Initially, the intensity ratio may increase due

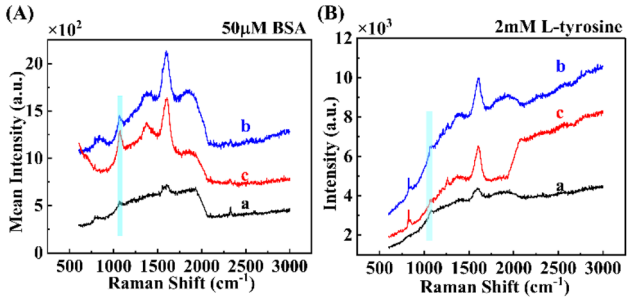

Fig. 5 UV-SERS spectra of (A) 50 μM BSA and (B) 2 mM L-tyrosine UV-SERS on samples a, b, and c after storage for 2.5 months.

to the formation of specific structures or oxidation products, followed by a decrease caused by excessive oxidation or structural disruption. These results indicate that the coverage of Rh NPs significantly influences the structural changes of BSA, thereby affecting the intensity ratios of peaks in the UV-SERS spectra. This emphasizes the crucial role of Rh NPs in regulating protein structure and SERS signals. To ensure that each scan covered the identical region, the scanning paths alternated between x [−10, 10] y [−10, 10] and x [10, −10] y [10, −10]. As shown in Fig. 4(D), the heatmap within the range of 1500 to 1700 cm^{-1} remains consistent across all four scans, confirming that the same area was repeatedly scanned.

We also conducted experiments to test 50 μM BSA on the same samples a, b, and c after storing them for 2.5 months to check the time stability of our substrates, and the result is reported in Fig. 5(A). To complement our UV-SERS measurements of BSA, we also examined the SERS spectra of L-tyrosine using the same samples a, b, and c, following the approach of the literature,[33] which highlighted the significant role of tyrosine residues in the UVRR spectra of BSA, while we only tested the UV-SERS spectra of 2 mM L-tyrosine dissolved in Milli-Q ultrapure water, and the result is presented in Fig. 5(B). By comparing the UV-SERS spectra of BSA and L-tyrosine in Fig. 5(A) and (B), we found that the spectra of these two substances are very similar. This also indicates that the significant role of tyrosine residues in the UVRR spectra of BSA, as highlighted in the literature, is also applicable to not-resonant UV-SERS.

Conclusions

In this work, we investigated, in detail, the performances, in terms of photostability effects, of a UV-plasmonic platform based on rough Al decorated with different concentrations of Rh NPs. While the combination of a porous Al film with Rh NPs has already been proved for applications in UV-SERS,[30] the analyses reported herein provide a better understanding of the behaviour of this particular plasmonic platform. In particular, using a suitable functionalization strategy to bring the probe molecules all over the sample, we verified that Rh NPs can facilitate the enhancement of the SERS signal. Not less interesting, we explored the effect of Rh NPs in the photostability under successive UV exposure discussing both oxidation effects and degradation effects in adenine and BSA. In particular, we discussed the potential role of hot carriers in the oxidation effect. As previously reported by Su *et al.*,[32] adenine can be modified to azupurine by charges generated in the plasmonic hot spots, due to the excitation of the plasmonic structures at energies close to the frequencies of localized surface plasmon resonance (LSPR). In our experiments with Al and Rh, it is known that the LSPR of Rh NPs falls in the UV spectral range (195–255 nm),[41] and hence, it is above 4.5 eV. In the case of aluminium, the 3s23p1 electronic states are located below the Fermi level, separated by small energy gaps of 0.5 eV and ∼1.6 eV, thus falling in the infrared region.[54] The 2p Al electronic state is located significantly below the Fermi level. In the case of rhodium, electron transitions from the 4d electronic state can be expected.[55] If we consider the whole system, that is contributions from both Rh and Al, the effect of hot electron generation is connected to the excitation of free electrons above the Fermi level (intraband transitions) or LSPR, and hot holes are present in the case of interband transitions. Nevertheless, they are significantly less mobile than electrons.[56,57] Therefore, a small number of hot holes in the bulk of the nanostructures reach the surface of the nanoparticles, but can still play a role in the oxidation of the molecules.

Overall, the results reported herein contribute to a better understanding of the UV-SERS phenomenon and can be extended to more efficient configurations such as nanoparticles on a mirror,[58–60] where the Rh NPs can be first functionalized with the probe molecules (for example DNA) and then deposited on an Al film.

Experimental

Sample preparation

Alfa Aesar 99.99% Al foil sheets were cut into squares of approximately 1 × 1 cm^2, with a thickness of 1.5 mm. The side not subjected to galvanic displacement was marked with a mechanical engraver.

After cutting, each sample was first washed with acetone and then with deionized water in an ultrasound bath (5 min) to remove any contaminants and dried. Subsequently, the sample was subjected to chemical etching in 5 M H_2SO_4 at 80 °C (5 min). After the chemical treatment, the square foils were treated with ultrasonics in water for an additional 5 minutes, dried only on the backside (where the marking is present), and deactivated with tape for anodization (3 M 8992). The GD processes were carried out using solutions prepared with deionized water (Elga-Veolia Purelab Pulse System, 18 MΩ cm) and high-purity reagents: NaCl (99.5%, Merck), $Na_3RhCl_6 \cdot 12H_2O$ (Alfa Aesar), and HCl (37%, Merck). To enhance the reproducibility – considering the slow equilibration of Rh chlorocomplex speciation[61,62] – the solutions were aged for 48 hours at 60 °C.

The solution, acidified to pH 2 with HCl, was kept at 25 °C and purged with nitrogen for 20 minutes prior to sample immersion.

After the galvanic exchange, the foils were washed in water, dried under a mild N_2 flow, and stored under vacuum pending morphological characterization (SEM).

Sample morphological characterization

Scanning electron microscopic (SEM) images were acquired using a Zeiss SIGMA microscope equipped with a field emission gun, operating under high vacuum at an accelerating voltage of 20 kV.

Image analysis performed using the open-source software ImageJ allowed for the estimation of the surface area fraction of Rh NPs covering the Al substrates.

Materials

Adenine (99%) and L-Tyrosine (99%) were purchased from J&K-Sci. BSA was purchased from Solarbio Life Science. NAD^+ (98%) was purchased from Shanghai Shaoyuan Co. Ltd. ATP (97%) and adenosine were purchased form Adamas-beta. All solutions were prepared using Milli-Q ultrapure water as the solvent.

Photostability tests with adenine

The substrates were dropped with 2 μL 0.5 mM adenine using a micropipette and tested after naturally drying at room temperature. For each mapping measurement, a small area of around 2×2 μm^2 (total 16 points for each scan) was used. The tests were performed in six consecutive scans for 0.5 mM adenine across the same small area with 10 s exposure time and one accumulation for each point. The same laser and acquisition parameters were maintaining the same for three samples. The raw spectra were baseline-corrected and smoothed using LabSpec6 (HORIBA measurement software) before processing averaged spectra and peak deconvolution analysis using Origin.

Photostability tests with BSA

Samples a, b, and c were dropped with 2 μL 15.1 μM adenine using a micropipette and subjected to tests after naturally drying at room temperature. For each mapping measurement, a total area of 20×20 μm^2 (total 16 points) with a step size of 6.667 μm was used. The tests were conducted in four consecutive scans across the same area with 10 s exposure time and one accumulation for each point. The same laser and acquisition parameters were maintaining the same for three samples. The raw spectra were baseline-corrected and smoothed using LabSpec6 (HORIBA measurement software) before processing averaged spectra and peak intensity analysis.

Raman spectroscopy

SERS measurements were conducted using a HORIBA LabRAM HR Evolution Raman spectrometer (Horiba Jobin Yvon, Kyoto, Japan) with a 40× UV objective and a 50× long-focal-length objective (NA = 0.75). The UV-SERS spectra of adenine, BSA and L-Tyrosine were recorded using a 325 nm laser at 10% power attenuation, 500-hole value and 1800 gr mm^{-1} grating with 10 s exposure time, and one accumulation. Thanks to the higher intensity of this laser with respect to the source at 266 nm used in our previous experiments, it has been possible to reduce the integration time in the spectra acquisition, thereby obtaining a more precise dynamics in the photodegradation.

The visible Raman spectra of bulk BSA were recorded using a 633 nm laser at 10% power, a 532 nm laser at 1% power and a 785 nm laser at 10% power with 600 gr mm^{-1} grating, 10 s exposure time, and one accumulation. For mapping measurements, the tests were conducted in six consecutive scans (small area total = 16 points for each scan) for 0.5 mM adenine and four consecutive scans (20×20 μm^2, total 16 points, 6.667 μm step size) for 15.1 μM BSA across the same area. The same laser and acquisition parameters were maintained for each measurement scan. For measuring 50 μM BSA, 2 mM L-tyrosine and several derivations of adenine on samples stored for 2.5 months, it is necessary to increase the acquisition time to 180 seconds with a single accumulation and 10% laser power. The spectra shown in Fig. 5 were obtained by averaging three randomly collected spectra without smoothing filter and baseline, and the abrupt changes at around 2000 cm^{-1} were due to rating alteration.

COMSOL multiphysics modelling

The electromagnetic field configurations produced by the Rh NPs on Al substrate was simulated using the wave optics module in COMSOL. Plane-wave excitation at 325 nm wavelength was used to obtain near-field distribution around Rh NPs of different sizes in partial-dome configurations (see ESI for detail†).

Data availability

Data for this article, including SEM micrographs and Raman spectroscopy data, are available at Zenodo at **https://doi.org/10.5281/zenodo.15436848**.

Author contributions

YZ, HJ, SW and QM performed the Raman measurements and data analysis; LM and SC conceived and performed the film synthesis; AD and GL performed sample characterizations; BJ and NM performed the numerical simulations; AD and GL supported in sample preparation; GA, KK, and NC supported data analysis and paper writing; and ZZ, SJ, and DG conceived the experiment and supervised the work. The authors thank the IIT clean room facility.

Conflicts of interest

There are no conflicts to declare.

Acknowledgements

The authors thank the National Natural Science Foundation of China (No.22202167), the National Key Research and Development Project of China (No. 2023YFF0613603), and the European Union under the Horizon 2020 Program, FET-Open: DNA-FAIRYLIGHTS, Grant Agreement 964995, the HORIZON-MSCA-DN-2022: DYNAMO, grant Agreement 101072818. NM and BJ acknowledge the 'Excellence by Choice' Programme at Umeå

University funded by Kempestiftelserna (grant no. JCK-2130.3). The authors thank the Clean Room Facility of IIT.

Notes and references

1 M. I. Stockman, K. Kneipp, S. I. Bozhevolnyi, S. Saha, A. Dutta, J. Ndukaife, N. Kinsey, H. Reddy, U. Guler, V. M. Shalaev, A. Boltasseva, B. Gholipour, H. N. S. Krishnamoorthy, K. F. Macdonald, C. Soci, N. I. Zheludev, V. Savinov, R. Singh, P. Groß, C. Lienau, M. Vadai, M. L. Solomon, D. R. Barton, M. Lawrence, J. A. Dionne, S. V. Boriskina, R. Esteban, J. Aizpurua, X. Zhang, S. Yang, D. Wang, W. Wang, T. W. Odom, N. Accanto, P. M. D. Roque, I. M. Hancu, L. Piatkowski, N. F. V. Hulst and M. F. Kling, *J. Opt.*, 2018, **20**, 043001, DOI: 10.1088/2040-8986/aaa114.

2 Y. Zou, H. Jin, Q. Ma, Z. Zheng, S. Weng, K. Kolataj, G. Acuna, I. Bald and D. Garoli, *Nanoscale*, 2025, **17**, 3656–3670.

3 D. Gerard and S. K. Gray, *J. Phys. D: Appl. Phys.*, 2015, **48**, 184001, DOI: 10.1088/0022-3727/48/18/184001.

4 J. M. McMahon, S. K. Gray and G. C. Schatz, *Phys. Rev. Lett.*, 2009, **103**, 097403.

5 T. Ding, D. O. Sigle, L. O. Herrmann, D. Wolverson and J. J. Baumberg, *ACS Appl. Mater. Interfaces*, 2014, **6**, 17358–17363.

6 P. Ponzellini, G. Giovannini, S. Cattarin, R. P. Zaccaria, S. Marras, M. Prato, A. Schirato, F. D'Amico, E. Calandrini, F. De Angelis, W. Yang, H.-J. Jin, A. Alabastri and D. Garoli, *J. Phys. Chem. C*, 2019, **123**, 20287–20296.

7 Y. Gutiérrez, R. Alcaraz de la Osa, D. Ortiz, J. M. Saiz, F. González and F. Moreno, *Appl. Sci.*, 2018, **8**, 64.

8 H. O. Everitt, Y. Gutierrez, J. M. Sanz, J. M. Saiz, F. Moreno, F. Gonzalez and D. Ortiz, *Opt. Express*, 2016, **24**, 20621.

9 A. Ahmadivand, R. Sinha, S. Kaya and N. Pala, *Plasmonics*, 2016, **11**, 839–849.

10 K. Appusamy, X. Jiao, S. Blair, A. Nahata and S. Guruswamy, *J. Phys. D: Appl. Phys.*, 2015, **48**, 184009, DOI: 10.1088/0022-3727/48/18/184009.

11 K. Watanabe, Y. Saito, M. Honda, Y. Kumamoto, S. Kawata and A. Taguchi, *ACS Photonics*, 2014, **1**, 598–603.

12 M. W. Knight, N. S. King, L. Liu, H. O. Everitt, P. Nordlander and N. J. Halas, *ACS Nano*, 2014, **8**, 834–840.

13 M. J. McClain, L. Zhou, S. Tian, O. Neumann, P. Nordlander, N. J. Halas, C. Zhang and X. Yang, *Nano Lett.*, 2017, **17**, 5071–5077.

14 J. Martin and J. Plain, *J. Phys. D: Appl. Phys.*, 2015, **48**, 184002, DOI: 10.1088/0022-3727/48/18/184002.

15 Z. Ahmed, M. Agio, Y. Ekinci, J. F. Löffler and S. K. Jha, *J. Am. Chem. Soc.*, 2012, **134**, 1966–1969.

16 A. N. Koya, X. Zhu, N. Ohannesian, A. A. Yanik, A. Alabastri, R. P. Zaccaria, R. Krahne, W. Shih and D. Garoli, *ACS Nano*, 2021, **15**, 6038–6060.

17 G. Ruffato, D. Garoli, S. Cattarin, S. Barison, M. Natali, P. Canton, A. Benedetti, D. D. Salvador and F. Romanato, *Microporous Mesoporous Mater.*, 2012, **163**, 153–159.

18 D. Garoli, E. Calandrini, G. Giovannini, A. Hubarevich, V. Caligiuri and F. D. Angelis, *Nanoscale Horiz.*, 2019, **4**, 1153–1157.

19 V. Caligiuri, H. Kwon, A. Griesi, Y. P. Ivanov, A. Schirato, A. Alabastri, M. Cuscunà, G. Balestra, A. De Luca, T. Tapani, H. Lin, N. Maccaferri, R. Krahne, G. Divitini, P. Fischer and D. Garoli, *Nanophotonics*, 2024, **13**, 1159–1167.

20 W. Yang, X.-G. Zheng, S.-G. Wang and H.-J. Jin, *J. Electrochem. Soc.*, 2018, **165**, C492–C496.

21 J. S. Corsi, J. Fu, Z. Wang, T. Lee, A. K. Ng and E. Detsi, *ACS Sustainable Chem. Eng.*, 2019, **7**, 11194–11204.

22 D. Garoli, A. Schirato, G. Giovannini, S. Cattarin, P. Ponzellini, E. Calandrini, R. Proietti Zaccaria, F. D'Amico, M. Pachetti, W. Yang, H.-J. Jin, R. Krahne and A. Alabastri, *Nanomaterials*, 2020, **10**, 102.

23 B. Nie, C. He and L. Liu, *J. Raman Spectrosc.*, 2013, **44**, 1512–1517.

24 M. Ardini, J. A. Huang, C. Sanchez-Sanchez, P. Ponzellini, N. Maccaferri, A. Jacassi, S. Cattarin, E. Calandrini and D. Garoli, in *SPIE Conf. Proceeding*, ed. T.Tanaka and D. P. Tsai, SPIE, 2017, p. 103460E.

25 A. Ahmadivand, R. Sinha, S. Kaya and N. Pala, *Plasmonics*, 2016, **11**, 839–849.

26 Y. Chen, Q.-S. Chen, S.-Y. Peng, Z.-Q. Wang, G. Lu and G.-C. Guo, *Chem. Commun.*, 2014, **50**, 1662–1664.

27 X. Zhang, P. Li, Á. Barreda, Y. Gutiérrez, F. González, F. Moreno, H. O. Everitt and J. Liu, *Nanoscale Horiz.*, 2016, **1**, 75–80.

28 P. Roy, S. Zhu, J.-B. Claude, J. Liu and J. Wenger, *ACS Nano*, 2023, **17**, 22418–22429.

29 M. Tran, S. Roy, S. Kmiec, A. Whale, S. Martin, S. Sundararajan and S. Padalkar, *Nanomaterials*, 2020, **10**, 644.

30 S. Banerjee, L. Mattarozzi, N. Maccaferri, S. Cattarin, S. Weng, A. Douaki, G. Lanzavecchia, A. Sapunova, F. D'Amico, Q. Ma, Y. Zou, R. Krahne, J. Kneipp and D. Garoli, *Mater. Adv.*, 2024, **5**, 6248–6254.

31 A. Barhoumi, D. Zhang, F. Tam and N. J. Halas, *J. Am. Chem. Soc.*, 2008, **130**, 5523–5529.

32 Y.-Q. Su, J. Liu, R. Huang, H.-T. Yang, M.-X. Li, R. Pang, M. Zhang, M.-H. Yang, H.-F. Su, R. Devasenathipathy, Y.-F. Wu, J.-Z. Zhou, D.-Y. Wu, S.-Y. Xie, B.-W. Mao and Z.-Q. Tian, *J. Phys. Chem. Lett.*, 2023, **14**, 5163–5171.

33 C. Spedalieri, J. Plaickner, E. Speiser, N. Esser and J. Kneipp, *Appl. Spectrosc.*, 2023, **77**, 1044–1052.

34 S. P. A. Fodor, R. P. Rava, T. R. Hays and T. G. Spiro, *J. Am. Chem. Soc.*, 1985, **107**, 1520–1529.

35 M. Pézolet, T. Yu and W. L. Peticolas, *J. Raman Spectrosc.*, 1975, **3**, 55–64.

36 W. L. Kubasek, B. Hudson and W. L. Peticolas, *Proc. Natl. Acad. Sci. U.S.A.*, 1985, **82**, 2369–2373.

37 V. Merk, E. Speiser, W. Werncke, N. Esser and J. Kneipp, *Appl. Spectrosc.*, 2021, **75**, 994–1002.

38 A. Y. Hirakawa, H. Okada, S. Sasagawa and M. Tsuboi, *Spectrochim. Acta, Part A*, 1985, **41**, 209–216.

39 R. P. Lopes, R. Valero, J. Tomkinson, M. P. M. Marques and L. A. E. Batista De Carvalho, *New J. Chem.*, 2013, **37**, 2691.

40 L. Cui, D.-Y. Wu, A. Wang, B. Ren and Z.-Q. Tian, *J. Phys. Chem. C*, 2010, **114**, 16588–16595.

41 A. M. Watson, X. Zhang, R. A. D. L. Osa, J. M. Sanz, F. González, F. Moreno, G. Finkelstein, J. Liu and H. O. Everitt, *Nano Lett.*, 2015, **15**, 1095–1100.
42 M. Pagliai, S. Caporali, M. Muniz-Miranda, G. Pratesi and V. Schettino, *J. Phys. Chem. Lett.*, 2012, **3**, 242–245.
43 T. Watanabe, O. Kawanami, H. Katoh, K. Honda, Y. Nishimura and M. Tsuboi, *Surf. Sci.*, 1985, **158**, 341–351.
44 B. Giese and D. McNaughton, *J. Phys. Chem. B*, 2002, **106**, 101–112.
45 H. Lang and Ch. Zimmer, *Photochem. Photobiol.*, 1979, **29**, 1083–1090.
46 A. Banyasz, T.-M. Ketola, A. Muñoz-Losa, S. Rishi, A. Adhikary, M. D. Sevilla, L. Martinez-Fernandez, R. Improta and D. Markovitsi, *J. Phys. Chem. Lett.*, 2016, **7**, 3949–3953.
47 H. G. Schulze, S. Rangan, M. Z. Vardaki, M. W. Blades, R. F. B. Turner and J. M. Piret, *Appl. Spectrosc.*, 2023, **77**, 957–969.
48 C. Heck, Y. Kanehira, J. Kneipp and I. Bald, *Molecules*, 2019, **24**, 2324.
49 S. Y. Cho, Y. S. Yun, S. Lee, D. Jang, K.-Y. Park, J. K. Kim, B. H. Kim, K. Kang, D. L. Kaplan and H.-J. Jin, *Nat. Commun.*, 2015, **6**, 7145.
50 S. Hashimoto, T. Yabusaki, H. Takeuchi and I. Harada, *Biospectroscopy*, 1995, **1**, 375–385.
51 N. Kuhar and S. Umapathy, *Anal. Chem.*, 2020, **92**, 13509–13517.
52 X. Dai, W. Fu, H. Chi, V. S. D. Mesias, H. Zhu, C. W. Leung, W. Liu and J. Huang, *Nat. Commun.*, 2021, **12**, 1292.
53 B. Fazio, C. D'Andrea, A. Foti, E. Messina, A. Irrera, M. G. Donato, V. Villari, N. Micali, O. M. Maragò and P. G. Gucciardi, *Sci. Rep.*, 2016, **6**, 26952.
54 H. J. Levinson, F. Greuter and E. W. Plummer, *Phys. Rev. B*, 1983, **27**, 727–747.
55 J. G. Gay, J. R. Smith and F. J. Arlinghaus, *Phys. Rev. B:Condens. Matter Mater. Phys.*, 1982, **25**, 643–649.
56 P. Lyu, R. Espinoza and S. C. Nguyen, *J. Phys. Chem. C*, 2023, **127**, 15685–15698.
57 R. Todorov and T. Hristova-Vasileva, *ACS Omega*, 2025, **10**, 19243–19255.
58 F. Benz, R. Chikkaraddy, A. Salmon, H. Ohadi, B. De Nijs, J. Mertens, C. Carnegie, R. W. Bowman and J. J. Baumberg, *J. Phys. Chem. Lett.*, 2016, **7**, 2264–2269.
59 E. J. Kluender, M. R. Bourgeois, C. R. Cherqui, G. C. Schatz and C. A. Mirkin, *J. Phys. Chem. C*, 2021, **125**, 12784–12791.
60 S. Mubeen, S. Zhang, N. Kim, S. Lee, S. Krämer, H. Xu and M. Moskovits, *Nano Lett.*, 2012, **12**, 2088–2094.
61 E. Verlato, S. Cattarin, N. Comisso, L. Mattarozzi, M. Musiani and L. Vázquez-Gómez, *Electrocatalysis*, 2013, **4**, 203–211.
62 L. Mattarozzi, S. Cattarin, N. Comisso, M. Musiani, L. Vázquez-Gómez and E. Verlato, *ChemElectroChem*, 2023, **10**, e202201122.